Nano Research
2022, 15(2): 1327–1337
ISSN 1998-0124 CN 11-5974/O4
https://doi.org/10.1007/s12274-021-3661-z

Research Article

Deterministic assembly of single emitters in sub-5 nanometer optical cavity formed by gold nanorod dimers on three-dimensional DNA origami

Zhi Zhao[1,3,4], Xiahui Chen[3], Jiawei Zuo[3], Ali Basiri[3], Shinhyuk Choi[3], Yu Yao[3], Yan Liu[1,2] (✉), and Chao Wang[1,3] (✉)

[1] *Center for Molecular Design and Biomimetics at the Biodesign Institute, Arizona State University, Tempe, Arizona 85287, USA*
[2] *School of Molecular Sciences, Arizona State University, Tempe, AZ 85287, USA.*
[3] *School of Electrical, Computer and Energy Engineering, Arizona State University, Tempe, AZ 85287, USA*
[4] *Faculty of Materials and Manufacturing, Key Laboratory of Advanced Functional Materials, Education Ministry of China, Beijing University of Technology, Beijing 100124, China*

Received: 4 May 2021 / **Revised:** 6 June 2021 / **Accepted:** 7 June 2021

ABSTRACT

Controllable strong interactions between a nanocavity and a single emitter is important to manipulating optical emission in a nanophotonic system but challenging to achieve. Herein a three-dimensional DNA origami, named as DNA rack (DR) is proposed and demonstrated to deterministically and precisely assemble single emitters within ultra-small plasmonic nanocavities formed by closely coupled gold nanorods (AuNRs). Uniquely, the DR is in a saddle shape, with two tubular grooves that geometrically allow a snug fit and linearly align two AuNRs with a bending angle < 10°. It also includes a spacer at the saddle point to maintain the gap between AuNRs as small as 2–3 nm, forming a nanocavity estimated to be 20 nm^3 and an experimentally measured *Q* factor of 7.3. A DNA docking strand is designed at the spacer to position a single fluorescent emitter at nanometer accuracy within the cavity. Using Cy5 as a model emitter, a ~ 30-fold fluorescence enhancement and a significantly reduced emission lifetime (from 1.6 ns to 670 ps) were experimentally verified, confirming significant emitter–cavity interactions. This DR-templated assembly method is capable of fitting AuNRs of variable length-to-width aspect ratios to form anisotropic nanocavities and deterministically incorporate different single emitters, thus enabling flexible design of both cavity resonance and emission wavelengths to tailor light–matter interactions at nanometer scale.

KEYWORDS

DNA origami, self-assembly, deterministic single emitter, plasmonic nanocavity, nanorod dimer, optical coupling

1 Introduction

The ability of nanophotonic structures to tailor and control light emission is highly attractive in enhanced imaging, data encryption, and ultra-compact circuitry [1–3]. One fundamental question is to control and strengthen the interaction between single quanta of light (photons emitted from an emitter) and single entities of matter (optical cavities) to engineer the optical coupling [4, 5]. For example, room-temperature (RT) quantum optics has been demonstrated by a number of methods [5–7], following an optical cavity design principle to maximize the "figure of merit" ($Q/\sqrt{V}$) [8], where *V* is the mode volume and *Q* is the cavity quality factor. A small *V* is favorable for enhancing the field-intensity and the coupling strength (*g*) of emitter in the cavity, while a large *Q* indicates a minimized energy loss. Given an emitter with an oscillator strength *f*, a maximal $Q/\sqrt{V}$ would lead to optimal coupling strength, as $g \propto f \cdot Q/\sqrt{V}$.

Traditionally, micro- or nano-structured dielectric cavities have been utilized for their high *Q* factors, such as micro-pillars [4], microdisks [9], and photonic crystals [6, 10, 11]. Recently, plasmonic nanocavities, such as nanowires [12], nanodisk dimers [7], and nanoparticles (cubes or spheres) coupled to a mirror have shown significant enhancement of coupling strength as a result of greatly reduced mode volume [13, 14]. However, it still remains challenging to achieve deterministic placement of single emitters in plasmonic or dielectric cavities in a reproducible manner.

To date, a number of methods had been proposed to align the emitter–cavity systems, including tip-based mechanical movement, aligning cavity on tracked emitters, etc. [15, 16]. Nevertheless, these methods relied on mechanical or lithographic alignments, making it impractical to achieve reproducible and accurate placement of an individual single emitter molecule within a nanometer-scale cavity. Additionally, the spatial alignment accuracy, even using advanced electron–beam system, was practically restricted to tens of nanometers. Over such a length scale, unfortunately, the electromagnetic wave distribution in nanophotonic cavities could change drastically, thus limiting fundamental studies and device applications.

DNA origami (DO) [17, 18], unlike conventional nano-patterning methods, enables bottom-up assembly to integrate organic emitters and plasmonic structures with nanometer accuracy at one step [19, 20]. During the assembly process,

Address correspondence to Yan Liu, Yan_Liu@asu.edu; Chao Wang, wangch@asu.edu

hundreds of short "staple" DNA strands can be programmed to fold a long scaffold strand into a relatively rigid structural template with a set of surface anchor strands at selective positions to specifically attach single-stranded-DNA-modified plasmonic nanoparticles and quantum emitters. The bottom-up self-assembly process eliminates complex and costly top-down alignment steps. Additionally, such a strategy allows emitters to be deterministically positioned in the cavity at nanometer precision [17] (e.g., 6 nm pixel size) that is well beyond the conventional lithographical capability [21, 22]. In one example, a nanocavity of a mode volume of ~ 200 nm^3 was achieved using surface coupled nanospheres [23]. In another demonstration, a gap of > 5 nm was formed between two gold nanospheres on a planar DO [24]. However, these demonstrations still had difficulties to achieve significant field enhancement and optical coupling at the single emitter level [23, 24], which was attributed to the design challenges on achieving small-mode-volume optical cavity and precisely placing a single emitter on the same DO template at the center of the nanocavity.

Herein we demonstrate deterministic placement of a single fluorescent emitter into the nanogap between a well-aligned gold nanorods (AuNRs) dimer assembled on a three-dimensional (3D) DO. This nanodevice displays highly enhanced emitter-cavity interactions due to improved optical coupling. The pair of AuNRs is aligned tip-to-tip at a close distance of about 2–3 nm via specifically designed saddle-shaped DO template featured with two tubular grooves, allowing geometrical snug fit to assemble two AuNRs with a specific width matching the inner dimension of the grooves. Such a design can greatly reduce mode volume, improve Q factor, and accordingly boost the coupling strength [25, 26]. Importantly, this DO template can accommodate AuNRs of the same diameter but varying lengths, and thus makes it possible to create nanocavities between a pair of AuNRs of different aspect ratios (AR) [27].

In this way, the cavity resonance wavelength is tuned to enable the systematic analysis of cavity-emitter interaction. Additionally, one single emitter labeled with single strand DNA (ssDNA) is incorporated precisely at the center of the AuNR dimer by hybridization with a programmed docking strand extending from the saddle point of the DO template. The positioning of the single emitter in the center of the nanocavity is expected to be within single digit nm precision. By incorporating Cy5 as the emitter, and using AuNR dimer of AR = 2.8 and width = 12 nm (effective mode volume ~ 20 nm^3), we demonstrated deterministic self-assembled coupling between plasmonic nanocavity and emitter with a high figure of merit $Q/\sqrt{V}$ (measured to be 1.6 nm$^{-3/2}$). We observed experimentally enhanced fluorescence emission (> 30 folds) and significantly reduced emission lifetime (from 1.6 ns down to 670 ps), compared with that of free Cy5 in solution.

2 Results and discussion

2.1 3D DNA origami template for assembly of AuNR nanocavities

Plasmonic nanocavities assembled from nanoparticles had been used for studying the cavity–emitter interactions [13, 14, 23, 24]. Maximizing the coupling strength between an emitter and the plasmonic nanocavity requires a few design considerations. First, in order to overcome the inevitable optical loss and reach the strong emitter–cavity coupling [13], the effective optical mode volume V_{eff} of the plasmonic nanocavity needs to be minimized, e.g., to as small as 10^{-6}. Herein V_{eff} is defined as $V_{\text{eff}} = V/V_\lambda = V \times (n/\lambda)^3$, where λ is the emission wavelength, n is the medium refractive index (RI), and V is the cavity optical mode volume. The minimization of V_{eff} can be achieved by reducing V to create an ultrasmall gap between the metallic nanoparticles as small as $\lambda/100$, e.g., 5 nm [13]. However, such a small gap size is challenging to achieve using conventional design and fabrication strategies (Table S1 in the Electronic Supplementary Material (ESM)). In particular, it is feasible to separate plasmonic nanoparticle dimers, or place nanoparticles on a metal mirror, with such a small distance via inserting a DO in between (Fig. S1 in the ESM), but the as-obtained gap sizes are constrained by the intrinsic dimensions of the double-stranded DNA (dsDNA) and the length of the linker molecules, thus it is challenging to achieve nanocavities with ultra-small (e.g., < 5 nm) dimensions [23, 24]. Moreover, most of the conventional methods cannot guarantee accurate and deterministic placement of the emitter to the nanocavity hotspot, which is essential for maximizing the emitter–cavity interaction.

Here, we address these challenges by employing a novel 3D DNA origami design, named as DNA rack (DR), to guide the assembly of single emitter precisely into the nanocavity formed by AuNRs with distances as small as 3 nm. The single emitter can be accurately and deterministically positioned at the nanocavity hotspot to maximize the emitter–cavity interaction. Moreover, our method allows tuning the plasmonic resonance of the nanocavities to match the emitter wavelength with minimal redesign efforts, which is also essential for strong enhancement of optical emission at a reduced V_{eff} [28, 29].

The DNA rack is a 3D DO template featuring two tubular grooves separated by a saddle-shaped spacer (Fig. 1(a)), which allows a geometrical snug fit of a pair of AuNRs of specific width, one in each groove, in order to both confine the orientation of AuNRs and define the gap size (Fig. 1(b)). In particular, AuNRs in a dimer were forced ~ 2 nm apart (tip to tip) by the steric effect of the DR geometry and specially designed spatial distribution of AuNR docking strands inside the grooves (Fig. S2 in the ESM). The deterministic placement of a single emitter at the center of the gap was achieved by docking one emitter-conjugated DNA strand to the complementary strand (strand

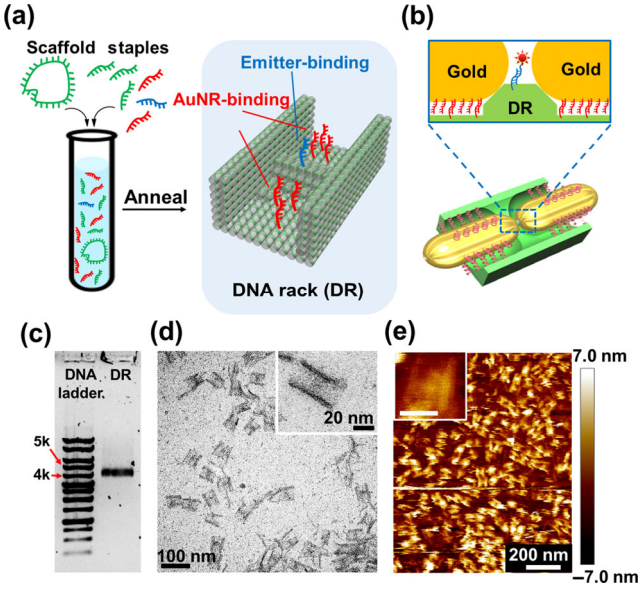

Figure 1 Design of DR and its application in constructing plasmonic nanocavities. (a) Simple scheme of the synthesis of DR. (b) 3D scheme of the design of anisotropic plasmonic optical cavity with a single emitter. Inset: side view of the nanocavity. (c) Agarose gel electrophoresis image of the purified DR samples. (d) TEM image of DR. Inset: a magnified single DR. (e) AFM image of DR. Inset: a magnified image of a single DR. Scale bar: 30 nm.

"docking" in Table S1 in the ESM) at the top-center position of the spacer by DNA hybridization. Here the "docking" stand was carefully designed, whose 3'-end protruded vertically to DR (Fig. 1(a)) and formed a 10-base-pair hybridization with the emitter-conjugated DNA strand. No single-stranded region was left in "docking". Thus we expected that the displacement of the emitter should be mainly from the dangling of the single-bond linker between the emitter and DNA. In our case, this moiety was short than 1 nm, which ensured the high placement accuracy of emitters.

The assembly of anisotropic plasmonic nanocavities using a AuNR dimer is more desirable compared with using dimers of gold nanosphere (AuNS) of the same volume and gap size. This is due to the following reasons as revealed by our finite-difference time-domain (FDTD) simulations (Fig. S3 in the ESM).

First, AuNS dimers (diameter 18 nm, gap 4 nm) provide only moderate field-enhancement factor $EF = |E / E_0|^2$, where E and E_0 are the intensity of electric field inside the nanocavity and in the incident light, respectively (Figs. S3(a) and S3(b) in the ESM). In comparison, the value of EF could reach an order of magnitude higher for a nanocavity formed by two coupled AuNRs (12 nm in diameter, 30 nm in length, and 4 nm in gap size) (Figs. S3(d)–S3(e) in the ESM).

Second, the plasmonic nanocavity formed by end-to-end coupled AuNR dimer is more advantageous in reducing non-radiative loss and enhancing light-matter interactions compared with AuNS dimers. Our simulation results (Figs. S3(e) and S3(d) in the ESM) showed the AuNR dimer possessed an ultra-small mode volume (V = 20 nm^3, see Section 4 for more detailed information), i.e., about 10 times smaller than that of AuNS dimers (200 nm^3), and an approximately twice as high Q factor in the calculation (14.6 for AuNR and 8.0 for AuNS).

Additionally, anisotropic nanocavity design also features greater flexibility to achieve a broad optical resonance tuning by simply changing the nanorod geometry, in particular its AR (Fig. S3(f) in the ESM) [30]. This allows programmable resonance detuning using one DR design, which is important to a systematic study of the coupled emitter–cavity system. In theory, the cavity resonance of coupled AuNR dimers could be tuned from 580 to over 780 nm by using AuNRs of a fixed width of 12 nm but varied lengths from 20 to 50 nm (Fig. S3(f) in the ESM). The actual resonance tuning accuracy may be limited by the deviation of AuNRs' size and assembly geometry, yet should be fairly enough for emitters with well separated emissions (e.g., tens of nm). This covers a series of widely used organic dyes, including Cy3, Cy5, Cy7, etc. [31]. In comparison, nanocavities formed by dimers of AuNSs with 20 to 50 nm in diameter display only minimal resonance change from 530 to 540 nm (Fig. S3(c) in the ESM), and thus their use could be limited by the availability of emitters for efficient coupling.

Furthermore, our simulation indicated that anti-crossing behavior with a hypothetical emitter (emission maximum at 773 nm, similar as Cy7) could only be observed in AuNR based anisotropic nanocavities (white arrow in Fig. S4(a) in the ESM), but not in AuNS based nanocavities (Fig. S4(b) in the ESM) using otherwise identical conditions.

Lastly, from the fabrication point of view, the same DR design could be directly used to assemble AuNRs of the same width but varying lengths (see the next section for more discussions), which greatly simplified both the design and experiments. In contrast, substantial modifications in the design would be necessary in order to assemble AuNSs of different diameters by using the same strategy to control a small inter-particle distance.

2.2 Assembly of AuNR nanocavities

The DR was designed with Cadnano 2.0 (Fig. S5(a) in the ESM) and prepared following the previously established annealing protocol [32]. Single-stranded, circular viral DNA from M13mp18 was utilized as the scaffold, which was folded by a total number of 217 staple strands into the designed 3D shape with well-defined dimensions. After annealing, the product was purified with a 100 kD Amicon micro-spin filter under centrifugation at 8,000 rpm for 10 min to remove the excess staple strands. Native agarose gel electrophoresis (GE) showed that the purified sample was a pure product, displaying a single migration band between 4k and 5k bp markers (Fig. 1(c)). The purified DR sample was further examined under transmission electron microscope (TEM), showing a high yield (~ 90%) and a morphology well matched to our design (Fig. 1(d)). For example, the measured length and width of DR were 57.5 ± 1.4 and 29.7 ± 0.9 nm, while the expected length and width from the design were 58.3 and 30.0 nm, respectively. The detailed features of the DR, e.g., the grooves and the central spacer, were visible in magnified TEM images (inset of Fig. 1(d)) and atomic force microscope (AFM) images (Fig. 1(e)). AFM line scans also revealed that the spacer was about 7 nm in height, which corresponded to 3 layers of dsDNA and well matched our design (Figs. S5(b) and S5(c) in the ESM). The width of the groove was measured to be ~ 23.1 ± 0.8 nm from TEM, slightly smaller than expected (25 nm), which could be attributed to possible tilting or curving of the DR.

To successfully assemble the DR-guided AuNR cavity with an optimal yield, the critical dimensions of the DR template and the AuNRs were designed to match. Herein we follow a previously developed synthetic strategy to prepare AuNRs of designed lengths and widths so they could fit the DR [33]. Briefly, a silver seed solution was added to a mixture containing $AgNO_3$ and $HAuCl_4$ for a controlled seeded-growth of AuNRs. By adjusting the concentrations of $HAuCl_4$ and $AgNO_3$, the width and length of the AuNRs could be tuned individually (Fig. S6 in the ESM). The successful preparation of a series of AuNRs of different ARs was confirmed by TEM imaging (Figs. 2(a)–2(d), Fig. S7 in the ESM), showing a relative standard deviation (SD) of 8%–9% in both length and width. Clearly, the tuning of the AuNR length from 30 (Figs. 2(a) and 2(c)) to 34 nm (Figs. 2(b) and 2(d)) did not affect the NR width and thus the assembly to DNA origami. AuNRs of 12 nm in width were chosen to construct the plasmonic nanocavities, whose geometry best fit the inner dimensions of the grooves of the DR.

To prepare the AuNRs for assembly with the DR, the AuNRs of the selected dimensions were surface-modified with a layer of 12-mer poly(T) capping strands, by incubating the AuNRs with thiol-terminated DNA capping strands and aging at elevated salt concentrations [34]. Ultraviolet–visible (UV–vis) spectra of the DNA modified AuNRs showed a small red shift with regard to the unmodified samples (Fig. S8 in the ESM), demonstrating the successful surface modification. NuPACK calculations indicated that such a capping strand could maintain a tight binding to its complementary strand below 45 °C, which is important to the formation and stability at RT. Although each nucleotide in a ssDNA was estimated to be ~ 0.56 nm long [35], the short persistent length of ssDNA (~ 2 nm) should make the capping layer flexible enough [36, 37] for the DNA-capped AuNRs to fit into the grooves on the DR. Upon hybridization to form dsDNA on the DR, the docking strands can be intuitively understood as rigid rods to bind AuNRs to the DR, considering a large persistent length of dsDNA of

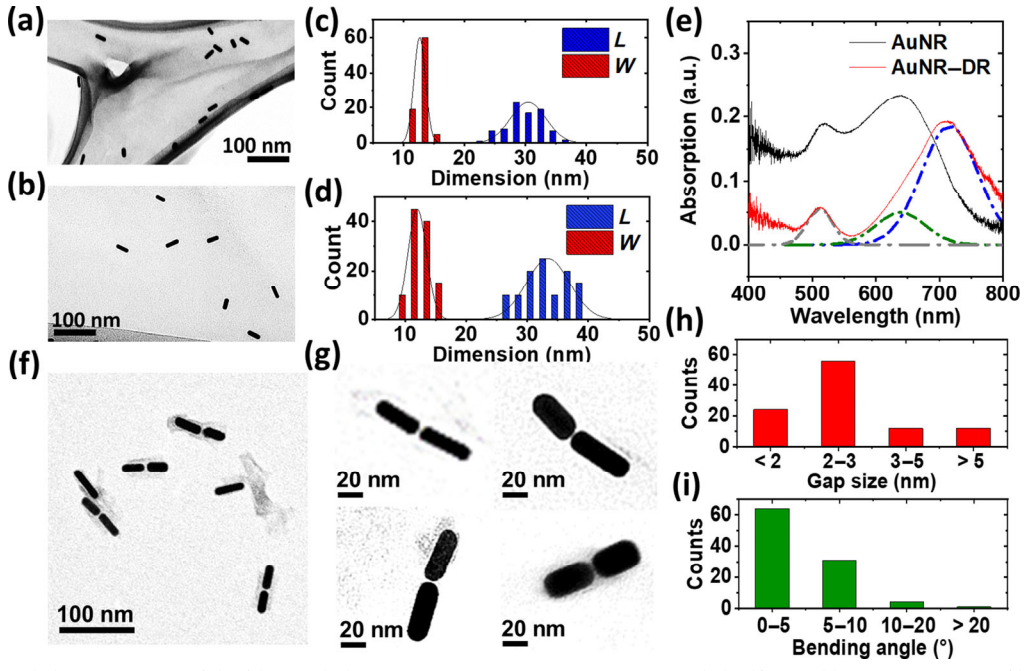

Figure 2 Structural characterization of the fabricated plasmonic AuNR nanocavities via DO guided self-assembly. (a) TEM image of home-synthesized AuNRs (AR = 2.5). (b) TEM image of home-synthesized AuNRs (AR = 2.8). (c) Size distributions of the AuNRs in (a). (d) Size distributions of the AuNRs in (b). (e) UV–vis spectra of AuNR monomers and AuNR dimer–DR complexes. The green and blue dashed lines correspond to the peak fitting result for the longitudinal plasmonic mode. (f) TEM image of fabricated AuNR–DR complexes. (g) Magnified TEM images of plasmonic nanocavity. (h) Distribution of the measured gap size in the nanocavities. (i) Distribution of the measured bending angle of the AuNR dimers.

~ 50 nm [38]. Such a rigidity is important to control of the DNA origami dimensions at nanometer scales. In our design, the longitudinal axis of AuNRs is estimated to be ~ 3 nm above the top of the spacer, so that the emitter is expected to be located at the center of the nanocavity gap, where the highest EF is expected (Fig. S3(d) in the ESM).

The DNA capped AuNR (e.g. AR = 2.8) was mixed with the purified DR, and subjected to multiple annealing treatments to assemble the plasmonic nanocavities. Fluorescence melting measurement (Fig. S9 in the ESM) indicated that the melting temperature of the AuNR docking strands hybridized with the complementary capping strands was around 42 °C, much lower than that of the DR (~ 62 °C). Therefore, the DR structure should remain intact during annealing. Here we set the starting annealing temperature at 45 °C, and slowly lowered it down to 30 °C in ~ 15 h. In order to facilitate the binding of AuNRs and the formation of AuNR linear dimers, the annealing cycle was repeated 4 times to obtain the most energetically stable product.

After annealing, the product was characterized with a microscope-coupled UV–vis spectrometer (Fig. S10 in the ESM). The working principle of each type of measurements is detailed in Section S5 in the ESM. The major absorption bands of the AuNR monomer peaked at 520 and 640 nm, which are the transversal and longitudinal plasmonic resonance modes, respectively (Fig. 2(e)), i.e., polarization along the short- and long-axis of the AuNRs. The AuNRs dimer product showed an additional band at 712 nm (the blue peak in Fig. 2(e)), representing the optical coupling of AuNRs from the small nanogaps and indicating the successful assembly of the AuNR dimers. Spectral deconvolution revealed a small peak at 640 nm (the green peak in Fig. 2(e)) from the assembly products, indicating a small percentage of remaining AuNR monomers. TEM images also revealed that AuNR dimers formed successfully (Fig. 2(f), Fig. S11 in the ESM).

The narrow gaps between the dimers were clearly visible from high-magnification TEM images (Fig. 2(g)). By analyzing the distribution of the gap sizes (AuNR tip to tip distance) from the images of hundreds of dimers (Fig. 2(h)), we found that the majority were smaller than 5 nm, and about a half were in the 2–3 nm range that was ideal for the investigation of cavity–emitter interaction. To the best of our knowledge, such a narrow gap size between plasmonic nanoparticles is one of the smallest achieved with DO templated assembly [39, 40], especially for tip-to-tip assembly of AuNRs. Moreover, the major portion (~ 95%) of the dimer possessed a near linear conformation ($\theta < 10°$), attributed partly to the high structural stability of the designed DR (Fig. 2(i)). The demonstrated high AuNR assembly accuracy of < 3 nm (Figs. 2(f)–2(i)) is favorable for studying emission enhancement and data analysis across different sample batches.

2.3 Surface immobilization of the AuNR dimer

The as-prepared AuNR–DR complexes were immobilized onto fused silica substrate through electrostatic interactions (Fig. 3(a)) for imaging and spectral characterizations. Following previously established protocols [11], the surface of the substrate was first modified with a negatively charged molecular species by carboxyethylsilanetriol disodium salt, which then associated with DR (negatively charged) under the presence of Mg^{2+} ions. Briefly, diluted AuNR–DR solution was drop-casted onto fused silica, incubated for 1 h, rinsed with copious amount of Tris buffer, and stabilized with high pH value (8.9), Mg^{2+} containing (15 mM) buffer. The as-prepared samples were examined under scanning electron microscope (SEM, Fig. S12 in the ESM), revealing successful immobilization of AuNR-DR complexes with a surface density of AuNR dimers ~ 0.5 per 1 μm^2. A small amount of AuNR monomers were also observed, attributed to the excessive AuNRs used during assembly, consistent with the UV–vis spectral analysis. Compared with their dimers, the AuNR monomer had a much lower surface density and would not be expected to significantly contribute to emission enhancement of the emitter or energy splitting, due to their much smaller field enhancement and resonance mismatch

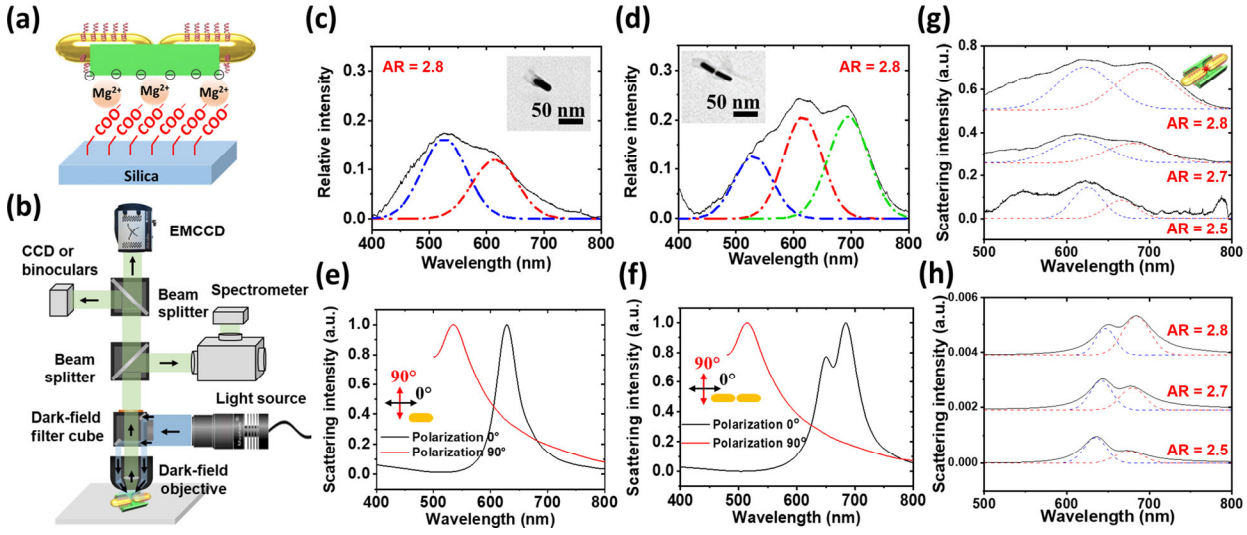

Figure 3 Dark field scattering characterizations of surface immobilized AuNR-DR complexes with assembled single emitters. (a) Scheme of the substrate immobilization mechanism. (b) Scheme of the experimental setup. Scattered light was collected by a spectrometer for spectral analysis. (c) and (d) DFS spectrum of the surface immobilized DR bound AuNR monomers (panel c) and dimers (panel d). The dash-dotted lines are the peak fitting results. Inset: representative TEM images of a DR bound AuNR monomer and dimer. The AuNRs are 12 nm in width and 30 nm long. (e) and (f) FDTD-calculated polarization-dependent DFS spectra of DR bound AuNR monomers (panel e) and dimers (panel f). The dimensions of AuNRs are the same as used in experiments (panels c and d). (g) The experimentally measured DFS spectra of plasmonic emitters made of AuNR dimers of various ARs. (h) Simulated DFS spectra of plasmonic quantum emitters made of AuNR dimers of various ARs.

(explained in detail in the next Section). Therefore, no extensive purification was conducted on the AuNR–DR complexes to avoid unnecessary sample loss. For control experiments, DR bound AuNR monomers were also prepared by removing the docking strands on one groove side of the DR (Fig. S13 in the ESM). The products were purified, immobilized and examined using the same procedures.

2.4 Microscopic and spectral characterization of optical emitters in anisotropic nanocavity

We employed dark field scattering (DFS) microscopy to characterize the nanocavity–emitter coupling (Fig. 3(b) and Section S6 in the ESM). The mechanism was schemed in Fig. S14 in the ESM. DFS spectra were each taken from a 62.5 μm × 62.5 μm area, which contained roughly 2,000 AuNR dimers, estimating from the SEM images.

Surface immobilized samples prepared with AuNRs of AR = 2.8 were first investigated as representatives. From the control sample, individual AuNRs (monomers on DR) with an emitter resulted in two resonance peaks in the DFS spectra (Fig. 3(c)), at ~ 525 and ~ 610 nm, respectively, corresponding to the transversal and longitudinal resonance mode of AuNR monomer. The blue-shifted longitudinal peak in DFS with regard to that in the solution (Fig. 2(e)) was due to the change in the refractive index of the media. On the other hand, the transverse resonance mode was mostly insensitive to the medium without significant change in resonance wavelength [41]. Different from AuNR monomers, AuNR dimers with an emitter exhibited more complex features from DFS spectra (Fig. 3(c)). The transverse mode (525 nm peak) remained visible despite being less evident, while additional peaks between 550 to 750 nm can be de-convoluted into two Gaussian peaks, centered around 622 and 695 nm, respectively.

To better understand the near-field coupling, we simulated DFS of surface immobilized AuNR–DR complexes using FDTD (Figs. 3(e) and 3(f)). The simulation results further confirmed that the experimentally observed scattering signals in 500–550 nm range (Figs. 3(c) and 3(d)) could be mainly attributed to the transverse mode for both the AuNR monomers and dimers. Since the AuNR dimer samples were randomly oriented during deposition, both the transvers mode and the longitudinal mode were excited in the experimental. However, the transverse mode was not expected to strongly interact with the dye given the large wavelength mismatch (> 140 nm) and poor near-field enhancement (only a few folds) (Fig. S15 in the ESM). In contrary, the longitudinal mode of the AuNR dimer resulted in the maximum electromagnetic field intensity in the center of the nanocavity (Fig. S3(d) in the ESM) with a small optical mode volume (20 nm^3), and optimal resonance of the nanocavity mode at the excitation and emission wavelengths of the emitter.

To study the interaction of Cy5 emitter with AuNR nanocavities, we varied the AR of AuNRs between 2.5 and 2.8 (Fig. 3(g)), and performed both DFS experiments and FDTD simulations (Figs. 3(g) and 3(h)). The DFS spectra in the range of 550–750 nm from both the experimental and the simulation data were fitted by two Gaussian peaks. As the AuNR AR increased, it was observed that the longer-wavelength peak gained intensity with regard to the shorter-wavelength peak. Meanwhile, the midpoint of the peak remained the same but the separation between the two peaks changed, thought due to the variation of resonance coupling between the cavity mode and the dye emission. This can be understood that a better match of the cavity resonance wavelength and the emission wavelength facilitated more efficient energy transfer between the emitted photons and the nanocavity, and accordingly decreased the non-radiative energy loss. Interestingly, the magnitude of energy difference between the two extracted peaks increased with a higher AuNR AR (Fig. 3(g)), possibly attributed to strong excitation of the emitters in the cavity. Yet, future experiments to more broadly tune the AuNR AR, as well as to increase the oscillator strength of emitters, are needed for more complete understandings of the emitter–cavity interactions [42].

These experimental observations were consistent with the FDTD simulations (Fig. 3(h)), where an AR dependent emitter–cavity coupling strength was evidenced. It is noticed that the experimental results displayed broader emission linewidths than that of the simulation, possibly due to the collective

scattering from many emitter–cavity systems (~ 2,000 emitters under a 62.5 μm × 62.5 μm field of view) with a geometrical variation of the AuNR dimers, e.g., length of the AuNRs, the gap size, and derivation from perfectly straight alignment. The observed phenomenon is thought to be correlated with anti-crossing behavior (Figs. S14 and S16 in the ESM); however, future work of single emitter analysis is needed to elucidate such an effect.

To further evaluate the impact of the plasmonic nanocavities on the emitter emission profiles, we investigated the fluorescence emission from Cy5 deterministically placed in the nanocavities using our customized microscope-coupled UV–vis spectrometer (Fig. 4(a), Section S5 in the ESM). For consistency, the same sample area (62.5 μm × 62.5 μm field of view) was used for fluorescence measurements following the DFS experiments. The spectral data clearly evidenced that a stronger fluorescence signal was recorded from surface immobilized AuNR dimers, compared to that of AuNR monomer or only DR (i.e., no AuNRs) (Fig. 4(b)). Due to the application of fluorescent filters (Section S5 in the ESM), only signals between 670 and 720 nm were collected, leading to the cutoffs in the spectra. It is noticed that AuNRs may display interband and intraband transitions due to hot carrier excitation at high illuminating laser power densities (0.1–0.2 MW/cm^2) [43]; however, such an effect is not expected to be dominant in our study given the relatively low power density produced by Xeon lamp (about 4 W/cm^2).

To quantify the overall fluorescence enhancement, the fluorescence signals between 670 and 720 nm were integrated (Fig. 4(c)), showing that the emitters inside the AR = 2.8 and AR = 2.5 AuNR dimer nanocavities were about 30 and 2 times brighter than that on the DR template only without the AuNRs, respectively (Section S7 in the ESM). This can be understood from simulation (Figs. 4(d) and 4(e)) that the use of AuNR dimers (AR = 2.8) resulted in a strong near-field enhancement at the nanocavities (dye-attachment site), reaching ~ 200 and ~ 900 folds at the absorption and emission maximum wavelengths of the dye, respectively. This relatively broad-band field enhancement overlapped well with both the emitter absorption and emission spectra, resulting in an enhanced excitation and an accelerated emission, simultaneously, and thus improved quantum efficiency [44, 45].

Further, the near-field enhancement of AR = 2.5 dimers over the data collection window was found 3 times lower than that of the AR = 2.8 nanocavities, showing that the AR = 2.5 dimers could enhance the dye excitation but not contribute significantly to promoting emission (Fig. 4(e)). This simulation results are consistent with the observed 90% lower fluorescence signal from AR = 2.5 dimer cavities.

Using the experimentally extracted geometric parameters from the TEM images, simulations were performed to calculate the near-field enhancement of the nanocavity at the emission wavelength (670 nm) for different AuNR ARs (Fig. S17 in the ESM), showing a maximum of 1.2 × 10^3 at AR = 2.8. Further, using AR = 2.8 AuNR dimer cavity as an example, the Q of the nanocavity was calculated as 14.6 and measured as 7.3, the mode volume was simulated as ~ 20 nm^3, and the Purcell factor was estimated 2.4 × 10^6 at dye emission (Section S8 in the ESM). This accordingly resulted in a large calculated $Q/\sqrt{V}$ value of 3.3 nm$^{-3/2}$ from simulation (or 1.6 nm$^{-3/2}$ using experimentally determined Q factor), which is up to two order of magnitude greater than plasmonic cavities formed by randomly placed nanoparticles and about one order of magnitude better than that of formed by DO templated assembly (Table S1 in the ESM). These analyses show that the AuNR nanocavities are a unique design strategy for maximizing the light matter interactions [46].

In contrast, Cy5 located close to the AuNR monomers did not

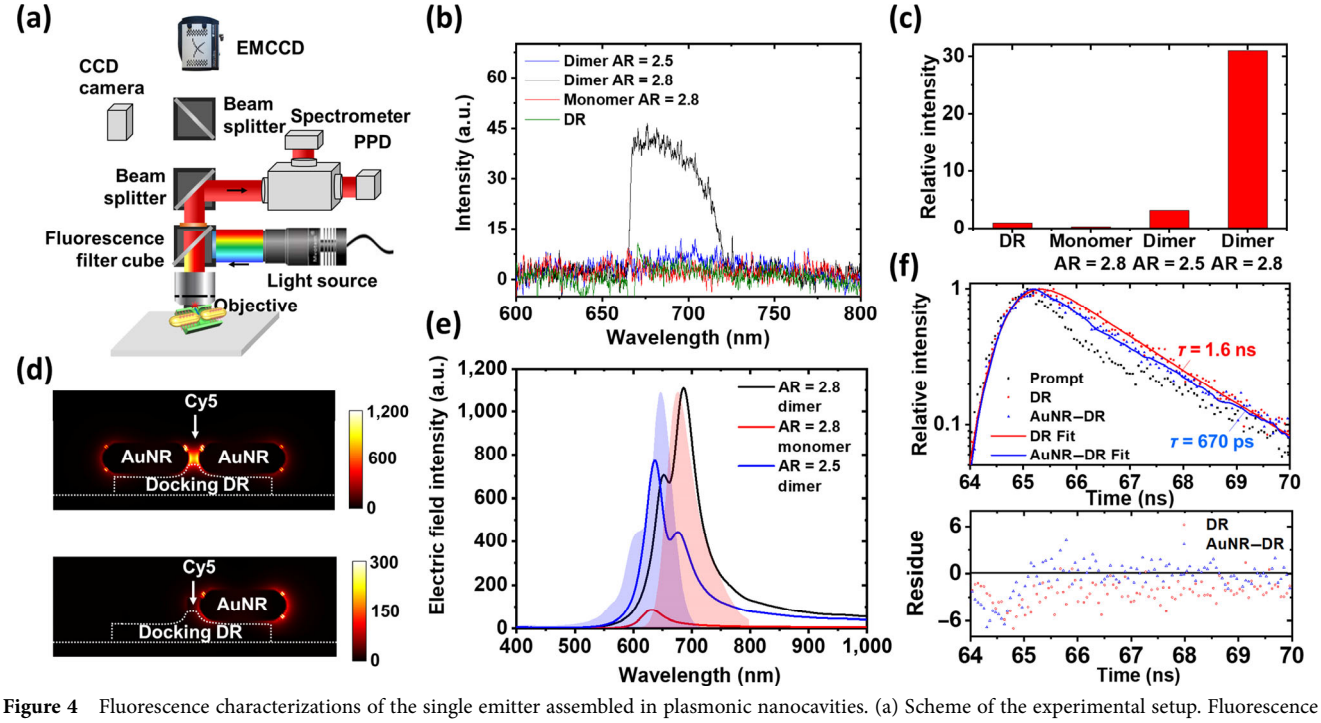

Figure 4 Fluorescence characterizations of the single emitter assembled in plasmonic nanocavities. (a) Scheme of the experimental setup. Fluorescence signals were collected by a spectrometer for spectral analysis or a PPD for lifetime measurements. (b) The measured fluorescence emission spectra of various samples. (c) Normalized fluorescence intensity of the samples in (b). (d) Simulated EF distribution in the vicinity of AR = 2.8 AuNR dimers (top) and AuNR monomers (bottom). The hotspots are clearly visible at the center spots of the AuNR dimer or close to the tips of the AuNR monomer. (e) Simulated electric field intensity as a function of wavelength at the nanocavity for both AuNR dimer and monomer. The Cy5 absorption and emission spectra were shown as shaded areas for comparison. (f) Fluorescence lifetime measurements and the corresponding residue of Cy5 with and without the plasmonic nanocavity.

display any observable fluorescence enhancement, compared with that from the dyes attached to DR only. Our simulation (Figs. 4(d) and 4(e)) showed that the field enhancement at the emitter site for the AuNR monomer was orders of magnitude smaller compared with that of AuNR dimers, i.e., ~ 75 and ~ 15 folds at the absorption and emission maxima, respectively. The small and narrow-band field enhancement as well as a larger resonance mismatch with regard to the emitter made the vicinity of AuNR monomer a much less effective nanocavity to overcome the fluorescence quenching due to nonradiative energy dissipation from the dye to the Au surface [47, 48], and therefore resulted in minimal overall enhancement of fluorescence signals [49]. Clearly, the presence of AuNP dimer nanocavity plays an important role in modulating the fluorescent emission process. Indeed, it has shown that Ag NPs can contribute to stabilize Cy3 or Cy5 dye molecules by promoting radiative decay channel and accordingly reducing the probability of photobleaching [50].

To better quantify the impact of AuNR nanocavity on the optical emission, the lifetime (τ) of the Cy5 dye with and without AuNRs was measured with a picosecond photon detector (PPD) device coupled to a spectrometer (Fig. 4(f)) and then analyzed using DAS6 software (Section S9 in the ESM). Under the presence of excessive decay pathways from the cavity, a reduced lifetime of the emitter from the excitation state to the ground state was expected [12]. The τ of Cy5 on the DR without AuNRs was 1.6 ns, comparable to but slightly longer than that of free Cy5 in aqueous buffers (1.2 ns) (Fig. S18 in the ESM), which was attributed to a stabilized fluorescence emission due to the attachment to DNA structures [51, 52]. When placed in the nanocavity, Cy5 was found to have a reduced lifetime of ~ 670 ps from mathematical fitting, due to optical coupling to the AuNR cavity. The fitting quality has been confirmed by minimal fitting residues as well as small deviations between experimental and calculated numbers (Fig. 4(f), and Fig. S19 in the ESM). This is consistent with the calculated large Purcell factor (~ 2.4×10^6), proving the effective modulation of optical emission. The reduced emission lifetime, attributed to cavity-enhanced emission, in turn is associated with higher photostability of dyes given possibly reduced quenching or photobleaching, as demonstrated before using Cy5-labeled DNA in the presence of metallic Ag particles [50].

3 Conclusions

In summary, we demonstrated a novel strategy to construct nanometer-scale plasmonic nanocavities via DNA origami guided AuNR self-assembly. The 3D morphology of DR enables a snug fit of AuNR dimers of designated widths with varying lengths, forming ultra-small nanocavities with a nanogap as small as 2 nm between a pair of linearly aligned AuNRs. The programmability of the DR allows placement of a single docking strand right at the center of the spacer, which could be used to deterministically attach a single emitter of chosen wavelength by DNA hybridization. A number of critical experimental parameters, including the concentration of reactants, annealing conditions, and AuNR geometries, were examined to produce AuNR dimers of varying plasmonic resonance peaks centered from 630 to 680 nm.

By using a single Cy5 dye deterministically placed in the nanocavity, we demonstrated that this new AuNR–DR complex can be used to study the interactions between single emitters and ultrasmall optical nanocavities. This system enabled us to detune the AuNR dimer resonance by varying their geometry parameters and observed the impact of the emitter on the AuNR dimer scattering. The AuNR dimer cavity was observed to enhance the Cy5 fluorescence emission by ~ 30 times, accompanied by a ~ 3 folds reduction of the emission lifetime. These observations were supported by our FDTD simulations that showed significant near-field enhancement, very small optical mode volume (20 nm^3), a large Purcell factor (as high as 2.4×10^6), and a large figure of merit $Q/\sqrt{V}$ of 3.3 $nm^{-3/2}$, all comparable to reported plasmonic nanocavity designs [13, 23].

This novel 3D DR design provides flexibility in AuNR assembly and emitter selection, making it a potential platform to study the strong interactions between single emitters and optical nanocavities. Future studies using emitters with a larger oscillator strength, such as quantum dots [42], and exploring plasmonic nanoparticle cavities of different geometries could potentially enable light-matter interactions in strong coupling regime. Besides fundamental studies, this new platform will be useful to a wide variety of applications, including enhanced fluorescence imaging, single-photon sources, quantum computing, etc.

4 Experimental

4.1 Materials

Ethylenediaminetetraacetic acid (EDTA, ACS grade), magnesium acetate tetrahydrate phenylbis (ACS grade), 2-amino-2-(hydroxymethyl)-1,3-propanediol (Tris base), sodium hydroxide (≥ 98%), boric acid (≥ 99.5%), gold(III) chloride trihydrate (≥ 99.9%), hexadecyltrimethylammonium bromide (CTAB, ≥ 99%), silver nitrate (ACS reagent, ≥ 99.0%), sodium borohydride (99%), L-ascorbic acid, agarose powder for molecular biology, and tris(2-carboxyethyl)phosphine hydrochloride (TCEP) were purchased from Sigma-Aldrich. Isopropyl alcohol, hydrochloric acid (36.5% to 38.0%), glacial acetic acid, Invitrogen™ 1 kb Plus DNA ladder, and Thermo Scientific™ 6x orange DNA loading dye were purchased from Fisher Scientific. Uranyl formate (UF, 99%–100%) was purchased from VWR. Carboxyethylsilanetriol disodium salt (CES, 25% in water) was purchased from Gelest. Fused silica was purchased from University Wafer. M13mp18 single-stranded DNA was purchased from New England Biolabs. All the staple strands were custom-synthesized by integrated DNA technologies (IDT) and received in the form of 200 μM solutions in 1× tris-EDTA (TE) buffer. All the other oligonucleotides were received in their lyophilized form from IDT. Their sequences are listed in Table S2 in the ESM.

4.2 Buffers

Tris-acetate EDTA (TAE) buffer was prepared as a 50× stock solution. The 50× stock solution was prepared by dissolving 242 g Tris base in water, adding 57.1 mL glacial acetic acid, and 100 mL of 500 mM EDTA (pH 8.0) solution, and bringing the final volume up to 1 liter. The stock solution was diluted 50 folds for experimental use. The 1× TAE buffer (40 mM tris, 20 mM acetate, 1 mM EDTA) that had been previously diluted from 50× stock solution might also be supplemented with 12.5 mM magnesium acetate tetrahydrate, herein referred to as 1× TAE/Mg^{2+}. Tris-phosphate-EDTA (TBE) buffer was prepared as a 10× stock solution. The stock solution was prepared by dissolving 108 g Tris base in water, adding 55 g of boric acid and 7.5 g EDTA, and bringing the final volume up to 1 liter. The stock solution was diluted to 1× for experimental use. Tris buffer was prepared by dissolving Tris base into deionized (DI) water and adjusting the pH with 1 M HCl. The final

concentration of Tris base was 10 mM with a pH of 8.3. The Tris-based stabilizing buffer was prepared in a similar manner. Tris base and magnesium acetate were first dissolved in DI water. The pH of the buffer was adjusted to 8.9. The final concentration of Tris and Mg^{2+} was 10 and 15 mM, respectively.

4.3 Preparation of DR

The DR was designed using Cadnano to include two tubular grooves and a "spacer" according to the geometry of home-synthesized AuNRs (Fig. S5(a) in the ESM). The overall dimension of DR was expected to be 58.3 nm (*L*) × 30.0 nm (*W*) × 15.0 nm (*H*), based on the known dimensions of DNA double helix: 3.4 nm long per 10.5 base pair (bp) and 2.5 nm wide per DNA helix (including the inter-helix gap) [18]. A group of 3 docking strands (AuL1_12–AuR3_12, see Table S2 in the ESM) were extended from selected helper strands on each side of the DR. These docking strands were expected to bind two DNA-decorated gold nanorods in a linear configuration via DNA hybridization. Another docking strand (emitter in Table S2 in the ESM) was designed at the top center of the spacer to tether DNA labeled dye molecule. The DNA structure was obtained by folding a circular single-stranded M13mp18 DNA with a set of short helper strands at 1:10 molar ratio in 1× TAE/Mg^{2+} buffer. The mixture solution was annealed in a thermocycler programmed for a cooling ramp from 90 to 25 °C over 12 h. The DNA labeled fluorescent dye (Cy5) was also incorporated during the annealing process. The assembled DR was purified with a 100 kD Amicon filter under centrifugation at 8,000 rpm for 10 min 3 times.

4.4 Characterization of DR

After purification, the correct intact structure of the DR was verified by gel electrophoresis, AFM, and TEM imaging while the concentration of the DR was estimated from the UV absorption at 260 nm. 1% agarose gel for GE tests was prepared by dissolving 1.00 g of agarose powder into 100 mL of 1× TBE buffer containing 2 μL of SYBR Safe DNA gel stain (Invitrogen). DO samples and DNA ladders were ran at 75 V for 35 min.

TEM images were taken with a Philips CM 12 microscope. Samples containing DNA origami were negatively stained with 1% UF for 30 s. AFM measurements were carried out with a Dimension FastScan system in the "ScanAsyst in fluid" mode using Scanasyst-Fluid+ tips (Bruker). For AFM imaging, 2 μL of the assembled sample was first diluted five times with 1× TAE/Mg^{2+} buffer, then 2 μL of diluted sample was deposited onto a freshly cleaved mica surface (Ted Pella), and 60 μL of 1× TAE/Mg^{2+} buffer was added on the top of the sample. After incubation for about 2 min to allow adsorption of the sample to the mica surface, the buffer solution was removed with a pipette. This also removed the most of the unbound helper strands to prevent their adverse effects on AFM imaging. Then 60 μL of buffer was added to the sample again, and an additional 60 μL was deposited on the AFM tip before engaging.

4.5 Synthesis of gold nanorod

The AuNRs were synthesized following a previous work with slightly modified recipes [33]. Briefly, 100 mM CTAB, 1 mM $AgNO_3$, and 79 mM ascorbic acid stock solutions were prepared first. $HAuCl_4$ was dissolved in 100 mM CTAB to yield a 1.5 mM $HAuCl_4$ stock solution. 60 μL of ice-cold 0.010 M $NaBH_4$ was quickly added to 1 mL 0.25 mM $HAuCl_4$ and 100 mM CTAB solution and vigorously stirred for 2 min. The solution should turn from dark yellow to brownish yellow immediately, which contained ~ 3.5 nm gold nanoparticles serving as seeds [33]. To synthesize AuNRs of various AR, desired amount of $AgNO_3$ solution, ascorbic acid solution, and $HAuCl_4$ stock solution of varying volume ratios were mixed. To that mixture, a certain amount of the seed solution was added. The detailed recipe is listed in Tables S3 and S4 in the ESM. The reaction mixture was then left undisturbed overnight to get the final products. The actual size of the as-synthesized AuNRs was characterized using a Philips CM 12 TEM. TEM images were analyzed by ImageJ.

4.6 Surface DNA modification of AuNRs

The AuNRs were modified with capping DNA sequences to pair with the docking DNA strands on the DO. The sequence of the capping DNA is listed in Table S2 in the ESM. To do the modification, dithiolated DNA was dissolved in DI water to yield a 1 mM solution. A 200 mM TCEP solution was prepared. The TCEP solution was mixed with DNA solution at equal volume and incubated at RT for 4 h during which the dithiol bond was reduced to -SH. The as-prepared DNA-SH was then purified with Amicon ultra centrifugal filters (3k MW cutoff) at 15k rpm for 10 min to remove excess TCEP and small molecules, and the concentration of DNA-SH was determined by measuring its absorption at 260 nm using a NanoDrop spectrometer (Thermo Scientific).

The synthesized AuNRs were purified by centrifugation at 9,000 rpm for 10 min four times to remove CTAB. The supernatant was discarded and the pellet was re-suspended in DI water. After the last spin, the pellet was dissolved in 1× TBE solution and 0.01% sodium dodecyl sulfate (SDS) was added. The concentration of the purified AuNR was determined by its maximum absorbance measured using UV–vis spectrometer (Bruker) assuming that an absorbance of 1 equaled to 0.4 nM. 100 μL 1 mM thiol-modified DNA strand was mixed with 1 mM 1 nM AuNR and the mixture was left at RT overnight. After that, 5 M NaCl was gradually added to the above mixture within 48 h to increase the salt concentration to 500 mM. The DNA modified AuNRs were purified by centrifugation at 8,000 rpm, 10 min for four times to remove excessive DNA and salts. The supernatant was replaced by a 1× TAE buffer (without Mg^{2+}) after each spin. After the last centrifugation, the concentration of the product was measured by UV–vis spectrometry and diluted to 1 nM with 1× TAE/Mg^{2+} buffer.

4.7 Preparation of AuNR-DR complexes

AuNRs and DR were self-assembled under thermal annealing. Fluorescence thermal curves were measured in optical tube strips using an MX3005P real-time thermocycler (Agilent Technology) equipped with a fluorescence 96-well plate reader. The DR was mixed with 1× SYBR Green I (Invitrogen) in 1× TAE/Mg^{2+} buffer. The fluorescence intensity of the emission was monitored at 522 nm with excitation at 495 nm at 1 min intervals. The samples were first heated to 85 °C for 10 min, and the temperature was reduced from 85 to 25 °C at a rate of −0.5 °C/min. After cooling down to 25 °C, the samples were held for 10 min and then heated to 85 °C with a temperature gradient of +0.5 °C/min. The thermal curve of AuNR capping strands binding with their complementary strands was measured using the same setup. Note the SYBR Green I dye only presented in melting curve measurements and was absent in other experiments. The DNA-capped AuNRs and the DR were mixed at a 3:1 molar ratio in 1× TAE/Mg^{2+} buffer. The mixture was then annealed from 45 to 30 °C at a rate of −0.02 °C/min. The annealing process was repeated 4 times to increase the final yield. For comparison, DR bound AuNR monomers were

also prepared by replacing the docking strands on one side (AuR1_12, AuR2_12, and AuR3_12 in Table S2 in the ESM) with the blocking strands (BR1_12, BR2_12, and BR3_12 in Table S2 in the ESM). The as-modified DR was only able to capture one AuNR inside one of its two grooves.

4.8 Modification of silica substrate

To enhance the affinity between the AuNR-DR complex and fused silica substrate, the surface of the silica was chemically modified with a layer of carboxyl groups. Fused silica chips were first cleaned by sonication (Branson 5800) in isopropyl alcohol (IPA) and DI water for 5 min, respectively. This step was repeated twice to remove most physically absorbed organic and inorganic contaminants. Next, the chips were dried in air and cleaned with 270 W oxygen plasma (Harrick Plasma expanded plasma cleaner) for 180 s. The chips were then immersed in the Tris buffer (pH 8.3) containing 0.01% CES for 10 min, followed by sonication in DI water.

4.9 Immobilization of AuNR-DO complexes

A 50 mm Petri dish was prepared with a moistened piece of laboratory tissue paper to limit evaporation. Solution with 100 pM AuNR–DR complexes was prepared in Tris buffer, and a 20 μL of drop was deposited in the middle of a fused silica chip. The chip was placed in the Petri dish, and the sample solution was allowed to incubate on the chip for 1 h with the Petri dish covered. After the incubation, excess sample in solution was washed away by 60 μL of fresh Tris buffer pipetted onto and taken off the chip, repeated 8 times. Next, the chip was again washed 8 times with the stabilizing buffer in order to allow the DO to bind strongly and to minimize artifacts during subsequent drying. The chip was finally dipped in 50% ethanol (v/v in water) for 10 s, 75% ethanol for 10 s, and 90% ethanol for 120 s. Then the chip was air-dried and ready for further tests.

4.10 Microscopic and spectral characterizations

The microscopic bright field imaging, dark field imaging, spectra collection, and lifetime analysis were performed using a customized optical system (Fig. S10 in the ESM). An upright Olympus BX53 microscope was equipped with a Xeon lamp (PowerArc, Horiba). The power density was measured to be 4.0 W/cm^2 after the objective. The sample-coated silica chips were illuminated, and bright filed images were recorded with a charge-coupled device (CCD) camera. Dark field images were taken using an electron multiplying CCD (EMCCD) camera (iXon Ultra, Andor) for enhanced sensitivity through 100× dark field lens (numerical aperture NA = 0.9). The detector was thermoelectrically cooled to −100 °C while the electron multiplication gain was set as 64. Spectral measurements were taken using a microscope-coupled UV–vis–near infrared (UV–vis–NIR) spectrometer (Horiba iHR 320) equipped with a CCD detector. Fluorescence lifetime was measured by a PPD 900 photo counting detector (Horiba) using SuperK EVO supercontinuum fiber laser (NKT Photonics) as the light source. The power density was measured to be 12.1 W/cm^2 after the objective. The integration was manually stopped when the measured peak height exceeded 1,000 counts, which commonly took 10–15 min for the surface immobilized emitters, and 3–4 h for the prompt signals. The region of interest on a sample was first found under bright field and dark field imaging mode. The dark field spectral data were then taken from the same region, followed by fluorescence measurements and lifetime measurements. Note that Cy5 might undergo photobleaching after continuous strong illuminations so the above optical measurements of a particular region were only conducted once. Lifetime value was extracted from the raw data using the DAS6 software from Horiba.

4.11 FDTD simulations

FDTD simulations were conducted with the commercial Ansys Lumerical software. The AuNR dimer was set with a width of 12 nm while the length varied in different simulations. The diameter of AuNS was set in such a way that its volume equaled to that of the AuNR in a parallel comparison. The gap between the AuNS or AuNR dimers was set as 4 nm. The complex refractive index ($\tilde{n}$) data of gold was defined following the experiment measured data of crystalline gold in literature [53]. The fused silica substrate material was modeled as Palik [53]. The $\tilde{n}$ of the background was set as 1. The docking DNA origami was modeled as a dielectric material with a constant $\tilde{n}$ of 1.53. The docking DNA origami was 58 nm long, 30 nm wide, and 6 nm tall. The Cy5 or Cy7 dye was modeled as a cube whose real part of $\tilde{n}$ (n) was 1.54 and the imaginary part (κ) was defined based on the absorption spectra of Cy5 and Cy7, respectively [51, 54]. Note the dye was a single molecule, whose extinction coefficient should differ from that of the bulk solution. Herein the maximum value of κ was set as 0.4. The effect of κ on the final scattering spectra is plotted in Fig. S20 in the ESM. The FDTD boundary condition was set as perfect matched layers (PML) in all directions (8 layers). The mesh size was set as 0.5 nm in x, y, and z directions in the area where AuNS or AuNR and the dye were located. Total field scattered field (TFSF) source was employed for scattering simulations. Five monitor planes were placed outside the TFSF source zone and covered both x, y directions, and positive z direction of the emitters in order to capture the scattering spectra.

Acknowledgements

Y. L. thanks the support from an Army Research Office MURI award no. W911NF-12-1-0420. C. W. thanks the ASU startup funds and National Science Foundation under grant Nos. 1711412, 1838443, and 1847324 for partially supporting this research. Y. Y. thanks the ASU startup funds and National Science Foundation under grant Nos. 1809997 for partially supporting this research.

Electronic Supplementary Material: Supplementary material (additional details on the experimental conditions, mathematical analysis on the fluorescence lifetime and Purcell factor, additional sample characterizations) is available in the online version of this article at https://doi.org/10.1007/s12274-021-3661-z.

References

[1] Tame, M. S.; McEnery, K. R.; Özdemir, Ş. K.; Lee, J.; Maier, S. A.; Kim, M. S. Quantum plasmonics. *Nat. Phys.* **2013**, *9*, 329–340.

[2] Thompson, J. D.; Tiecke, T. G.; De Leon, N. P.; Feist, J.; Akimov, A. V.; Gullans, M.; Zibrov, A. S.; Vuletić, V.; Lukin, M. D. Coupling a single trapped atom to a nanoscale optical cavity. *Science* **2013**, *340*, 1202–1205.

[3] Faraon, A.; Fushman, I.; Englund, D.; Stoltz, N.; Petroff, P.; Vučković, J. Coherent generation of non-classical light on a chip via photon-induced tunnelling and blockade. *Nat. Phys.* **2008**, *4*, 859–863.

[4] Andreani, L. C.; Panzarini, G.; Gérard, J. M. Strong-coupling regime for quantum boxes in pillar microcavities: Theory. *Phys. Rev. B* **1999**, *60*, 13276–13279.

[5] Minder, M.; Pittaluga, M.; Roberts, G. L.; Lucamarini, M.; Dynes, J. F.; Yuan, Z. L.; Shields, A. J. Experimental quantum key distribution beyond the repeaterless secret key capacity. *Nat. Photon.* **2019**, *13*, 334–338.

[6] Hennessy, K.; Badolato, A.; Winger, M.; Gerace, D.; Atatüre, M.; Gulde, S.; Fält, S.; Hu, E. L.; Imamoğlu, A. Quantum nature of a strongly coupled single–quantum–dot–cavity system. *Nature* **2007**, *445*, 896–899.

[7] Schlather, A. E.; Large, N.; Urban, A. S.; Nordlander, P.; Halas, N. J. Near-field mediated plexcitonic coupling and giant Rabi splitting in individual metallic dimers. *Nano Lett*. **2013**, *13*, 3281–3286.

[8] Reithmaier, J. P.; Sęk, G.; Löffler, A.; Hofmann, C.; Kuhn, S.; Reitzenstein, S.; Keldysh, L. V.; Kulakovskii, V. D.; Reinecke, T. L.; Forchel, A. Strong coupling in a single quantum dot-semiconductor microcavity system. *Nature* **2004**, *432*, 197–200.

[9] Srinivasan, K.; Painter, O. Linear and nonlinear optical spectroscopy of a strongly coupled microdisk–quantum dot system. *Nature* **2007**, *450*, 862–865.

[10] Thon, S. M.; Rakher, M. T.; Kim, H.; Gudat, J.; Irvine, W. T. M; Petroff, P. M.; Bouwmeester, D. Strong coupling through optical positioning of a quantum dot in a photonic crystal cavity. *Appl*. *Phys*. *Lett*. **2009**, *94*, 111115.

[11] Gopinath, A.; Miyazono, E.; Faraon, A.; Rothemund, P. W. K. Engineering and mapping nanocavity emission via precision placement of DNA origami. *Nature* **2016**, *535*, 401–405.

[12] Akimov, A. V.; Mukherjee, A.; Yu, C. L.; Chang, D. E.; Zibrov, A. S.; Hemmer, P. R.; Park, H.; Lukin, M. D. Generation of single optical plasmons in metallic nanowires coupled to quantum dots. *Nature* **2007**, *450*, 402–406.

[13] Chikkaraddy, R.; De Nijs, B.; Benz, F.; Barrow, S. J.; Scherman, O. A.; Rosta, E.; Demetriadou, A.; Fox, P.; Hess, O.; Baumberg, J. J. Single-molecule strong coupling at room temperature in plasmonic nanocavities. *Nature* **2016**, *535*, 127–130.

[14] Hoang, T. B.; Akselrod, G. M.; Argyropoulos, C.; Huang, J. N.; Smith, D. R.; Mikkelsen, M. H. Ultrafast spontaneous emission source using plasmonic nanoantennas. *Nat*. *Commun*. **2015**, *6*, 7788.

[15] Van Der Sar, T.; Hagemeier, J.; Pfaff, W.; Heeres, E. C.; Thon, S. M.; Kim, H.; Petroff, P. M.; Oosterkamp, T. H.; Bouwmeester, D.; Hanson, R. Deterministic nanoassembly of a coupled quantum emitter-photonic crystal cavity system. *Appl*. *Phys*. *Lett*., **2011**, *98*, 193103.

[16] Riedrich-Möller, J.; Arend, C.; Pauly, C.; Mücklich, F.; Fischer, M.; Gsell, S.; Schreck, M.; Becher, C. Deterministic coupling of a single silicon-vacancy color center to a photonic crystal cavity in diamond. *Nano Lett*. **2014**, *14*, 5281–5287.

[17] Rothemund, P. W. K. Folding DNA to create nanoscale shapes and patterns. *Nature* **2006**, *440*, 297–302.

[18] Han, D. R.; Pal, S.; Nangreave, J.; Deng, Z.; Liu, Y.; Yan, H. DNA origami with complex curvatures in three-dimensional space. *Science* **2011**, *332*, 342–346.

[19] Samanta, A.; Zhou, Y. D.; Zou, S. L.; Yan, H.; Liu Y. Fluorescence quenching of quantum dots by gold nanoparticles: a potential long range spectroscopic ruler. *Nano Lett*. **2014**, *14*, 5052–5057.

[20] Pal, S.; Dutta, P.; Wang, H. N.; Deng, Z. T.; Zou, S. L.; Yan, H.; Liu, Y. Quantum efficiency modification of organic fluorophores using gold nanoparticles on DNA origami scaffolds. *J*. *Phys*. *Chem*. *C* **2013**, *117*, 12735–12744.

[21] Xin, L.; Lu, M.; Both, S.; Pfeiffer, M.; Urban, M. J.; Zhou, C.; Yan, H.; Weiss, T.; Liu, N.; Lindfors, K. Watching a single fluorophore molecule walk into a plasmonic hotspot. *ACS Photon*. **2019**, *6*, 985–993.

[22] Vietz, C.; Kaminska, I.; Paz, M. S.; Tinnefeld, P.; Acuna, G. P. Broadband fluorescence enhancement with self-assembled silver nanoparticle optical antennas. *ACS Nano* **2017**, *11*, 4969–4975.

[23] Chikkaraddy, R.; Turek, V. A.; Kongsuwan, N.; Benz, F.; Carnegie, C.; Van De Goor, T.; De Nijs, B.; Demetriadou, A.; Hess, O.; Keyser, U. F. et al. Mapping nanoscale hotspots with single-molecule emitters assembled into plasmonic nanocavities using DNA origami. *Nano Lett*. **2018**, *18*, 405–411.

[24] Roller, E. M.; Argyropoulos, C.; Högele, A.; Liedl, T.; Pilo-Pais, M. Plasmon-exciton coupling using DNA templates. *Nano Lett*. **2016**, *16*, 5962–5966.

[25] Lin, K. Q.; Yi, J.; Hu, S.; Liu, B. J.; Liu, J. Y.; Wang, X.; Ren, B. Size effect on SERS of gold nanorods demonstrated via single nanoparticle spectroscopy. *J*. *Phys*. *Chem*. *C* **2016**, *120*, 20806–20813.

[26] Huang, C. P.; Yin, X. G.; Kong, L. B.; Zhu, Y. Y. Interactions of nanorod particles in the strong coupling regime. *J*. *Phys*. *Chem*. *C* **2010**, *114*, 21123–21131.

[27] Jain, P. K.; Eustis, S.; El-Sayed, M. A. Plasmon coupling in nanorod assemblies: optical absorption, discrete dipole approximation simulation, and exciton-coupling model. *J*. *Phys*. *Chem*. *B* **2006**, *110*, 18243– 18253.

[28] Funston, A. M.; Novo, C.; Davis, T. J.; Mulvaney, P. Plasmon coupling of gold nanorods at short distances and in different geometries. *Nano Lett*. **2009**, *9*, 1651–1658.

[29] Shao, L.; Woo, K. C.; Chen, H. J.; Jin, Z.; Wang, J. F.; Lin, H. Q. Angle-and energy-resolved plasmon coupling in gold nanorod dimers. *ACS Nano* **2010**, *4*, 3053–3062.

[30] Link, S.; Mohamed, M. B.; El-Sayed, M. A. Simulation of the optical absorption spectra of gold nanorods as a function of their aspect ratio and the effect of the medium dielectric constant. *J*. *Phys*. *Chem*. *B* **1999**, *103*, 3073–3077.

[31] Süel, G. Use of fluorescence microscopy to analyze genetic circuit dynamics. *Methods Enzymol*. **2011**, *497*, 275–293.

[32] Liu, X. G.; Zhang, F.; Jing, X. X.; Pan, M. C.; Liu, P.; Li, W.; Zhu, B. W.; Li, J.; Chen, H.; Wang, L. H. et al. Complex silica composite nanomaterials templated with DNA origami. *Nature* **2018**, *559*, 593–598.

[33] Gole, A.; Murphy, C. J. Seed-mediated synthesis of gold nanorods: Role of the size and nature of the seed. *Chem*. *Mater*. **2004**, *16*, 3633–3640.

[34] Mirkin, C. A.; Letsinger, R. L.; Mucic, R. C.; Storhoff, J. J. A DNA-based method for rationally assembling nanoparticles into macroscopic materials. *Nature* **1996**, *382*, 607–609.

[35] Cocco, S.; Marko, J. F.; Monasson, R. Theoretical models for single-molecule DNA and RNA experiments: From elasticity to unzipping. *C R Phys*. **2002**, *3*, 569–584.

[36] Roth, E.; Azaria, A. G.; Girshevitz, O.; Bitler, A.; Garini, Y. Measuring the conformation and persistence length of single-stranded DNA using a DNA origami structure. *Nano Lett*. **2018**, *18*, 6703–6709.

[37] Chi, Q. J.; Wang, G. X.; Jiang, J. H. The persistence length and length per base of single-stranded DNA obtained from fluorescence correlation spectroscopy measurements using mean field theory. *Phys*. *A Stat*. *Mech*. *Appl*. **2013**, *392*, 1072–1079.

[38] Hagerman, P. J. Flexibility of DNA. *Annu*. *Rev*. *Biophys*. *Biophys*. *Chem*. **1988**, *17*, 265–286.

[39] Thacker, V. V.; Herrmann, L. O.; Sigle, D. O.; Zhang, T.; Liedl, T.; Baumberg, J. J.; Keyser, U. F. DNA origami based assembly of gold nanoparticle dimers for surface-enhanced Raman scattering. *Nat*. *Commun*. **2014**, *5*, 3448.

[40] Simoncelli, S.; Roller, E. M.; Urban, P.; Schreiber, R.; Turberfield, A. J.; Liedl, T.; Lohmüller, T. Quantitative single-molecule surface-enhanced Raman scattering by optothermal tuning of DNA origami-assembled plasmonic nanoantennas. *ACS Nano* **2016**, *10*, 9809–9815.

[41] Chang, W. S.; Ha, J. W.; Slaughter, L. S.; Link, S. Plasmonic nanorod absorbers as orientation sensors. *Proc*. *Natl*. *Acad*. *Sci*. *USA* **2010**, *107*, 2781–2786.

[42] Moreels, I.; Lambert, K.; De Muynck, D.; Vanhaecke, F.; Poelman, D.; Martins, J. C.; Allan, G.; Hens, Z. Composition and size-dependent extinction coefficient of colloidal PbSe quantum dots. *Chem*. *Mater*. **2007**, *19*, 6101–6106.

[43] Cai, Y. Y.; Liu, J. G.; Tauzin, L. J.; Huang, D.; Sung, E.; Zhang, H.; Joplin, A.; Chang, W. S.; Nordlander, P.; Link, S. Photoluminescence of gold nanorods: Purcell effect enhanced emission from hot carriers. *ACS Nano* **2018**, *12*, 976–985.

[44] Fort, E.; Grésillon, S. Surface enhanced fluorescence. *J*. *Phys*. *D*: *Appl*. *Phys*. **2007**, *41*, 013001.

[45] Giannini, V.; Fernández-Domínguez, A. I.; Heck, S. C.; Maier, S. A. Plasmonic nanoantennas: Fundamentals and their use in controlling the radiative properties of nanoemitters. *Chem*. *Rev*. **2011**, *111*, 3888–3912.

[46] Purcell, E. M. Spontaneous emission probabilities at radio frequencies. In *Confined Electrons and Photons*. Burstein, E.; Weisbuch, C., Eds.; Springer: Boston, 1995; pp 839.

[47] Kinkhabwala, A.; Yu, Z. F.; Fan, S. H.; Avlasevich, Y.; Müllen, K.; Moerner, W. E. Large single-molecule fluorescence enhancements

produced by a bowtie nanoantenna. *Nat*. *Photon*. **2009**, *3*, 654–657.
[48] Rose, A.; Hoang, T. B.; McGuire, F.; Mock, J. J.; Ciracì, C.; Smith, D. R.; Mikkelsen, M. H. Control of radiative processes using tunable plasmonic nanopatch antennas. *Nano Lett*. **2014**, *14*, 4797–4802.
[49] Geddes, C. D.; Lakowicz, J. R. Editorial: Metal-enhanced fluorescence. *J*. *Fluoresc*. **2002**, *12*, 121–129.
[50] Malicka, J.; Gryczynski, I.; Fang, J. Y.; Kusba, J.; Lakowicz, J. R. Photostability of Cy3 and Cy5-labeled DNA in the presence of metallic silver particles. *J*. *Fluoresc*. **2002**, *12*, 439–447.
[51] Yoshie, T.; Scherer, A.; Hendrickson, J.; Khitrova, G.; Gibbs, H. M.; Rupper, G.; Ell, C.; Shchekin, O. B.; Deppe, D. G. Vacuum Rabi splitting with a single quantum dot in a photonic crystal nanocavity. *Nature* **2004**, *432*, 200–203.
[52] Moreira, B. G.; You, Y.; Owczarzy, R. Cy3 and Cy5 dyes attached to oligonucleotide terminus stabilize DNA duplexes: Predictive thermodynamic model. *Biophys*. *Chem*. **2015**, *198*, 36–44.
[53] Olmon, R. L.; Slovick, B.; Johnson, T. W.; Shelton, D.; Oh, S. H.; Boreman, G. D.; Raschke, M. B. Optical dielectric function of gold. *Phys*. *Rev*. *B* **2012**, *86*, 235147.
[54] Carmichael, H. J.; Brecha, R. J.; Raizen, M. G.; Kimble, H. J.; Rice, P. R. Subnatural linewidth averaging for coupled atomic and cavity-mode oscillators. *Phys*. *Rev*. *A* **1989**, *40*, 5516–5519.